J Mater Sci (2010) 45:2823–2838
DOI 10.1007/s10853-010-4251-8

REVIEW

Application of nanostructured porous silicon in the field of optics. A review

V. Torres-Costa · R. J. Martín-Palma

Received: 11 November 2009 / Accepted: 19 January 2010 / Published online: 12 February 2010

Abstract Porous silicon nanostructures have attracted a great deal of interest during the past few years, due to their many remarkable properties. The high-efficiency visible photo- and electro-luminescence of this material opened the way to the development of silicon-based optoelectronic devices fully compatible with standard industry processes. In addition to these luminescent properties, nanostructured porous silicon shows a variety of other interesting properties, including tunable refractive index, low light absorption in the visible, high internal surface, variable surface chemistry, or high chemical reactivity. All these properties, along with its ease of fabrication and the possibility of producing precisely controlled layered structures make this material adequate for its use in a wide range of fields, such as optics, micro- and optoelectronics, chemical sensing or biomedical applications, for example. This article reviews the applications of nanostructured porous silicon that exploit its unique optical properties, as in the case of light emitting devices, filtered photodetectors, optical sensors, and others.

Introduction

Communications and information processing needs have been growing exponentially during the last few decades, and this is pushing the microelectronics technology toward its limits. For this reason, increased interest is being devoted to photonics, a technology where electron currents are substituted by light beams, and would allow faster and broader band transmission of information. A fully photonic communications system would allow the multiplexed transmission of huge amounts of information at higher speeds and with lower power consumption than its electronic counterpart. For that purpose, highly integrated photonic devices are required to produce, process, transmit, and receive light with high efficiency.

Microelectronics industry has been dominated by silicon, probably becoming the best-known material to man. An unprecedented technological and industrial capacity has developed around silicon since the invention of the transistor and hence, it is expected that silicon be the base of this new photonic technology. Unfortunately, as any other indirect gap semiconductor, silicon's radiative transitions have very low efficiency (around 10^{-6}). Current solutions include the usage of highly efficient direct-gap semiconductors, such as GaAs, InP, and several other III–V and II–VI compounds. However, these materials are expensive and, most importantly, do not allow their direct integration into current silicon technology. In this respect, it would be desirable to develop a silicon-based or at least silicon-compatible material with the appropriate photonic properties that could be easily integrated in the current CMOS technology standards.

Within this context, an article by Canham [1] published in 1990 raised a great deal of interest, since strong visible photoluminescence at room temperature from p-type silicon wafers electrochemically etched in HF-based solutions was reported. The photoluminescent emission was attributed to quantum confinement effects from the resulting nanostructured porous silicon (nanoPS) layers. Additionally, the emission wavelength was shown to be easily tunable throughout the visible and infrared ranges by simply selecting the appropriate fabrication conditions. Soon afterwards, Halimaoui et al. [2] reported electroluminescent

V. Torres-Costa (✉) · R. J. Martín-Palma
Departamento de Física Aplicada, Universidad Autónoma de Madrid, 28049 Cantoblanco, Madrid, Spain
e-mail: vicente.torres@uam.es

emission of similar characteristics during the formation of nanoPS, and Koshida and Koyama [3] reported the successful fabrication of solid-state electroluminescent devices based on this material. The discovery of the photo- and electroluminescent properties of nanoporous silicon opened the way to the development of silicon-based optoelectronic devices fully compatible with standard CMOS processes.

Since Canham's article in 1990, more than 15,000 articles related to porous silicon (PS) have been published according to the Web of Knowledge [4]. However, PS is by no means a new material. In fact, PS was first obtained by Uhlir [5] at Bell Laboratories in 1956 when studying electropolishing of silicon and germanium in HF-based solutions. It was reported that electropolishing was only achieved for anodization currents above a certain threshold value. For currents below that threshold, the result was regarded as a brownish deposit of some silicon suboxide. In the early 1970s, this deposit was identified as a silicon porous structure [6], and during the 1980s, PS was used in silicon-on-insulator (SOI) technology to produce high-quality thick oxide layers [7].

In addition to its luminescent properties, PS shows a wide variety of other interesting properties leading to applications in several fields ranging from micro- and optoelectronics to biomedical applications. Under the appropriate formation conditions, PS layers with feature sizes in the nanometer range are fabricated (nanoPS). In this case, the characteristic feature sizes are well below the wavelength of infrared and visible light. Accordingly, in this wavelength range, nanoPS can be regarded as an homogeneous effective medium, whose optical properties mainly depend on porosity, which is easily controlled during the fabrication process. Also, the high internal surface of nanoPS is of great importance for certain applications. Moreover, the high reactivity of this surface makes the physico-chemical properties of nanoPS very sensitive to its environment. Thus, changes in the optical, electrical, or chemical properties of nanoPS can be used to develop a number of devices, including chemical and biological sensors.

Fabrication and general properties

Since the early works by Uhlir [5] and Turner [8], nanoPS has been generally fabricated by the electrochemical etch of monocrystalline silicon in ethanoic HF solutions, although stain etching in HF/HNO_3 solutions has also been used for specific applications [9]. Some other techniques have been proposed, including vapor phase etching [10], spark processing [11], and chemical etching in organic solvents [12]. The electrochemical method has been demonstrated to be easily scalable to process up to 8″ wafers aiming at the production of large area homogeneous PS layers [13], rendering this technique suitable for industrial optics or solar cell applications of PS, for example. This review will be focused on nanoPS fabricated by the electrochemical etch of Si wafers in HF-based solutions. This is the most widely used and versatile method for the fabrication of PS with feature sizes in the nanometer range.

Although the mechanism responsible for the electrochemical dissolution of silicon in HF-based solutions has not been satisfactorily explained yet, the most widely accepted model for p-type silicon was proposed by Allongue et al. [14], and is schematically depicted in Fig. 1. Initially, the surface Si atoms are passivated with hydrogen [12, 15]. The weak Si–H bonds are broken and substituted with Si–OH bonds, taking two holes in the process. In the next step, F^- ions replace OH^- groups, yielding Si–F bonds. These ionic bonds induce a strong polarization on the Si atoms, weakening their backbonds with the other Si atoms. The weakened Si–Si bonds are then attacked by HF molecules, tearing the Si atom apart from the bulk, and leaving the remaining Si atoms (now at the surface) bound to H atoms. The process then continues from the beginning until it is interrupted.

The previously described reaction mainly depends on the availability of holes to initiate the process. The silicon/electrolyte interface can be regarded as a Schottky diode, in which holes arising from bulk Si reach the electrolyte crossing the spatial charge region (the PS layer) by thermoionic effect [16]. Surface irregularities due to missing Si atoms produce a concentration of current lines at the pore tips, lowering the barrier height and enhancing the process there. As a consequence, the porous structure is depleted of carriers, becoming more resistive [17]. Additionally, as the silicon structures become smaller, the semiconductor band gap widens due to quantum confinement effects [1]. This effect becomes prominent when the confinement reaches the exciton Bohr radius (6 nm in the case of silicon). These two effects enhance the accumulation of holes at the pore tips, thus enhancing the dissolution process at these points and promoting the in-depth growth of pores. Another key consequence of such growth mechanism is that the already formed porous structure is not further affected by the continuation of the etching process, which is of tremendous importance for the fabrication of homogeneous PS layers and multilayers, especially for large thicknesses.

Given that during the dissolution process of bulk silicon the availability of holes plays a decisive role, it becomes apparent that such parameters as current density and doping level have a great influence on the resulting structure and properties of PS. Other parameters such as electrolyte composition (mainly HF concentration), crystalline orientation, or process temperature, also influence the reaction kinetics and hence the morphology of PS. Even the presence of light during the process has an important effect on the

final structure; it provides the required holes for PS formation in the case of n-type silicon, and reduces the typical feature size in the case of p-type Si wafers, as a consequence of the increased hole concentration given by the creation of electron–hole pairs. As a result, an ample variety of structures, porosity, and pore morphology may be achieved depending on the fabrication parameters [18]. Some of the most representative structures are presented in Fig. 2.

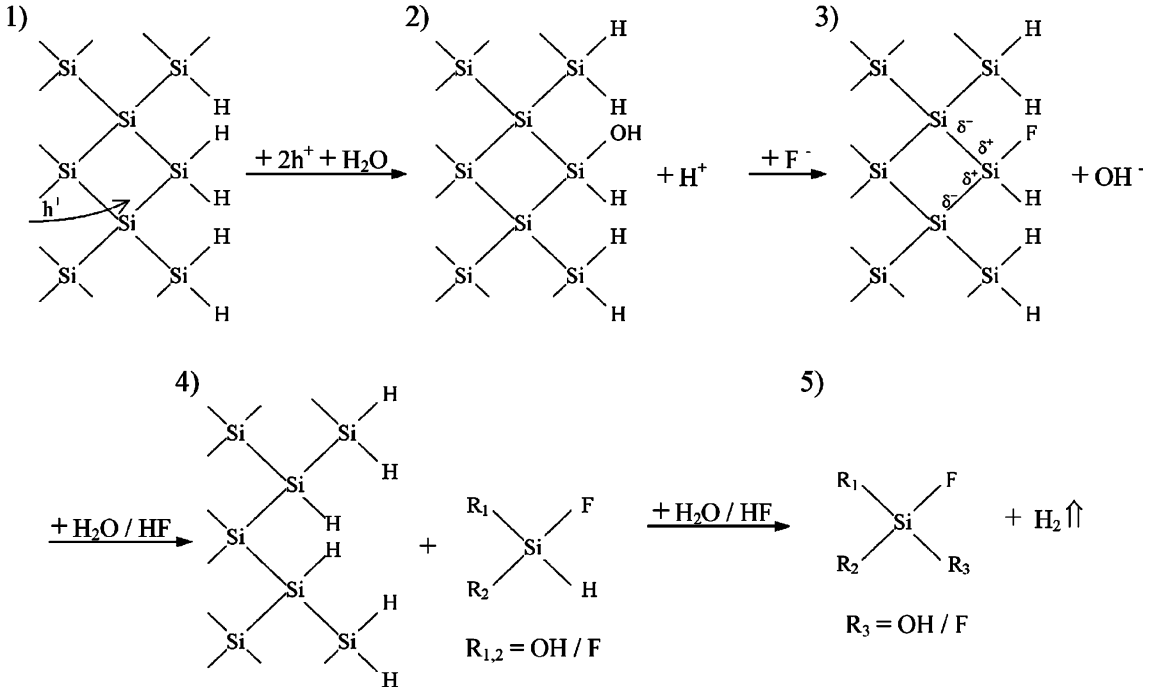

Fig. 1 Schematic representation of the electrochemical dissolution of silicon leading o the formation of porous silicon. Adapted from [14]

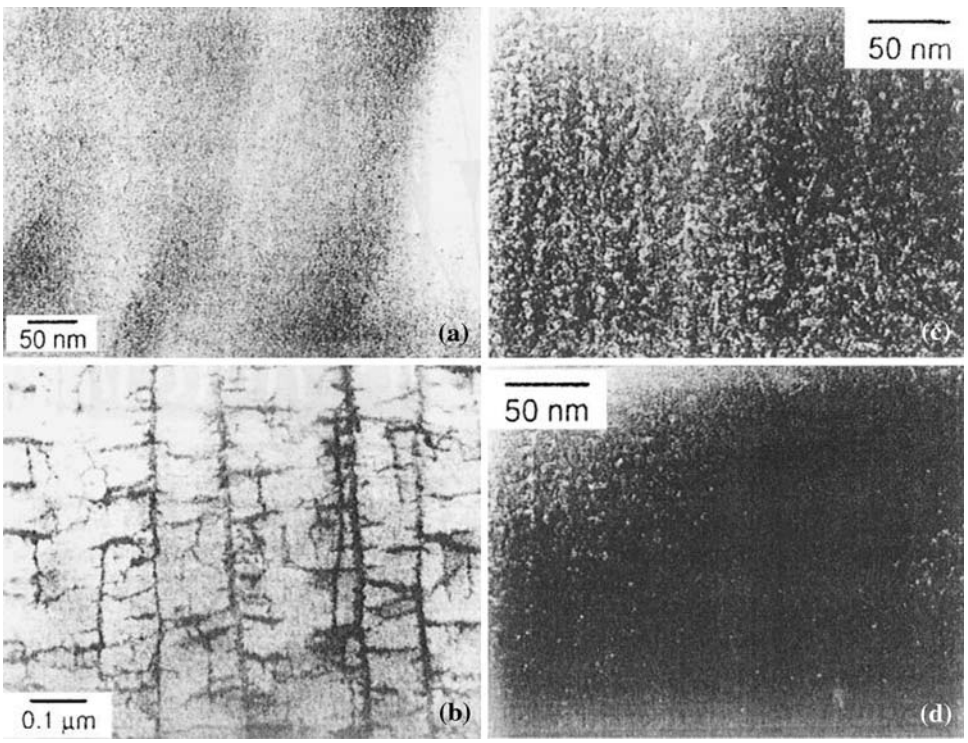

Fig. 2 Summary of different morphologies and structures of porous silicon. Reprinted from [18]. Copyright 1992 American Institute of Physics

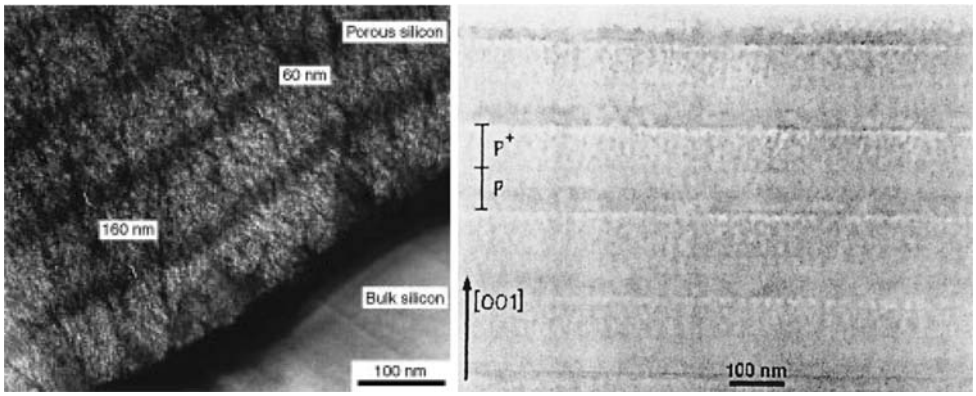

Fig. 3 Cross-sectional transmission electron microscopy (TEM) images of porous silicon multilayer stacks, obtained by varying the current density during formation (*left*, from [71] with kind permission from Springer Science + Business Media) and by using an epitaxially grown substrate (*right*, reprinted from [22] with permission from Elsevier)

As previously stated, the silicon skeleton is depleted of carriers after pore formation [1, 19], which means that the etching process takes place only at the pore tips without affecting the porous structure already formed. Accordingly, a change in the etching parameters only affects the structure currently being formed, resulting in a new layer of different characteristics beneath the already formed one and yielding a bi-layer structure. This process may be repeated several times resulting in complex multilayer structures. The most extended method for the fabrication of multilayer structures consists on changing the applied current density with time, i.e., by alternatively switching the anodization current between low and high values a stratified structure of low- and high-porosity layers, respectively, is obtained [18, 20]. A cross-sectional view of a typical multilayer structure fabricated by this method is shown in Fig. 3—left. In a similar way, alternate light intensities can be used to obtain multilayer structures in n-type silicon [21]. A more precise method, but also considerably more complex and expensive, consists on the etching under constant conditions of epitaxially grown wafers with given doping profiles. Given the high sensitivity of the etching process to the dopant level [22], a multilayer structure is obtained following the initial dopant depth profile, as shown in Fig. 3—right.

Porous silicon single layers

Structure and morphology

For any intended optical and optoelectronic application of PS, it is mandatory to ensure the good quality of the layers and interfaces resulting from the electrochemical etching process. In particular, good layer homogeneity, both lateral and in-depth, and sharp interfaces are required to achieve optimal optical properties. The precise determination of etch rates for each set of fabrication parameters is also

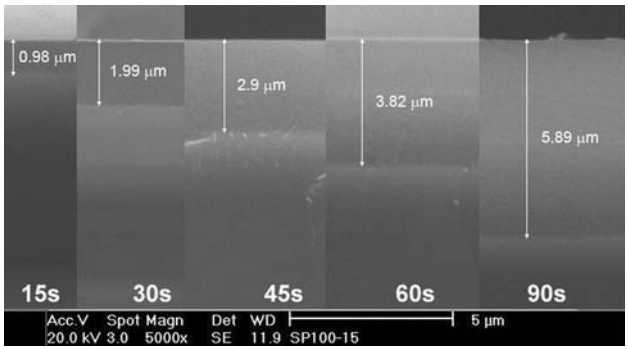

Fig. 4 Cross-sectional SEM images of nanoPS layers formed under the same situations, for increasing etching times. Reproduced from [48]

required in order to precisely control the thickness of the individual layers. Electron microscopy images, such as the one presented in Fig. 4, show that thickness increases linearly with etch time for a given current density, indicating that the process takes place at a constant etch rate [16, 21] (Fig. 5).

However, this is much more complex since the etch rate is greatly influenced by several parameters including crystal orientation, doping density, and electrolyte composition, among others. Highest etch rates are obtained for <100> oriented wafers, since in this case the pore growth is perpendicular to the surface, and depends almost linearly on the anodization current density for p-type wafers [22, 23]. Higher doping levels also increase the etch rates due to enhanced injection of holes in the case of p-type silicon. In contrast, for n-type wafers the etch rate is less sensitive to the doping level, since holes are provided by illumination. Figure 6 exemplifies the influence of the etch rate for different wafer types and initial resistivity.

Morphological characterization of PS has been carried out in the last two decades with a wide variety of techniques. Raman spectroscopy and X-ray diffraction, for example, have been extensively used to determine the

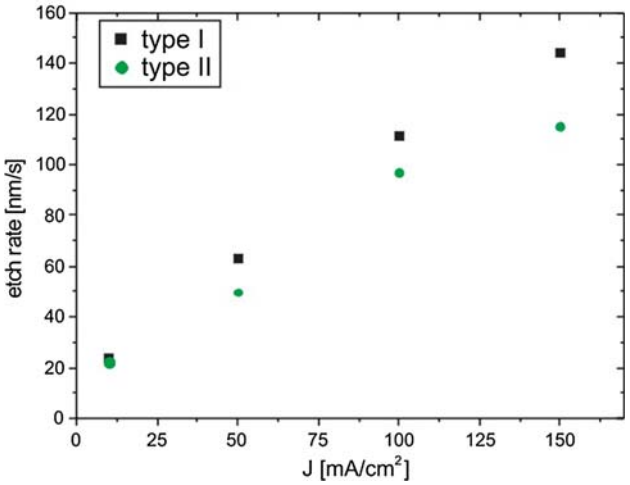

Fig. 5 Dependence of etch rate with current density for two different HF concentrations, from [57] with kind permission from Springer Science + Business Media

degree of crystallinity and crystallite size [24–34]. High-resolution transmission electron microscopy (HRTEM) has been used to study the structural properties of PS, as well as the size and lattice parameter of silicon nanocrystals [35–38], while high-resolution scanning electron microscopy has been widely used to study surface morphology, pore size, and in-depth homogeneity. The experimental results show that, under the appropriate experimental conditions (typically p^+ silicon wafers and HF concentration in the 20–50% range), PS layers with controlled feature sizes (pore diameter, crystallite size) well below 50 nm can be easily obtained. As a consequence, in the visible and infrared wavelength ranges, this particular type of PS will behave as an optically homogeneous medium, since radiation wavelengths are much larger than these characteristic sizes.

In-depth homogeneity and sharp PS/silicon interfaces are two important requirements for the fabrication of structures with good optical properties. The interface of PS with bulk silicon has also been studied by HRTEM [39] (Fig. 7), finding a dark stripe along the PS/Si interface, which can be attributed to diffraction effects due to the presence of a stress field [39–41].

The presence of a low-porosity transition layer at the PS/Si interface has also been detected by Rutherford backscattering spectroscopy (RBS) [42] and Raman spectroscopy. In particular, Raman measurements have shown the existence of a transition layer at the interface with a high density of dislocations and compressive stresses as high as 13 kbar [43]. The existence of these dislocations has been directly observed with HRTEM [42] (Fig. 7d). It is believed that these dislocations allow the adjustment of the mismatching lattice parameters of PS and bulk silicon [44, 45]. These observations support the hypothesis that these interfacial dislocations are the result of a lattice relaxation process to accommodate the vacants originated after the dissolution of silicon atoms during the etching process. These dislocations show quite high-electronic activity that enhances the electrochemical silicon dissolution. Thus, defect-free regions retain their crystallinity, which leads to the formation of silicon nanocrystals embedded in an amorphous matrix surrounded by dislocations [39, 43]. In this way, this interfacial region observed by HRTEM and Raman is related to the first stages of the silicon dissolution process, which is interrupted when the etching process is stopped.

Another important characteristic of p-type nanoPS that makes it suitable for optical applications is its low-surface roughness. Values below 1 nm of RMS roughness have been measured by atomic force microscopy [46–48], as shown in Fig. 8, and may reach 1.5 or 2 nm for high-porosity layers.

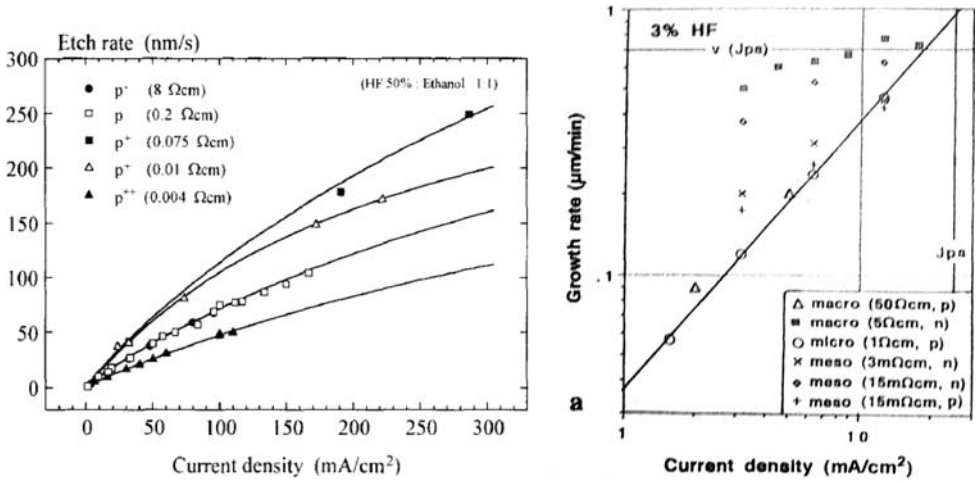

Fig. 6 Influence of etch rate for different wafer type and resistivity. *Left*: reprinted from [22] with permission from Elsevier. *Right*: reproduced from [23] with permission

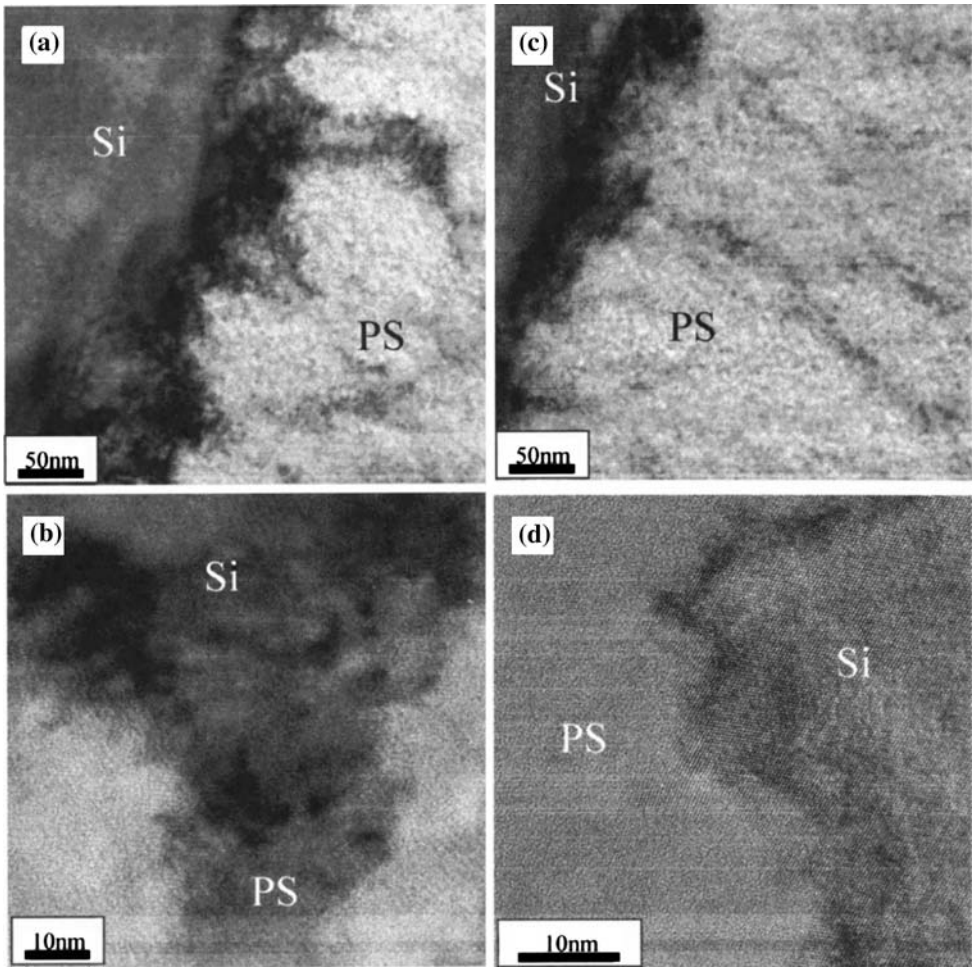

Fig. 7 HRTEM images of the PS/Si interface for two different anodization current densities: 40 mA/cm^2 (**a**, **b**) and 80 mA/cm^2 (**c**, **d**). Reprinted with permission from [39]. Copyright 2004, American Institute of Physics

According to the Davies–Bennett model [49, 50], the amount of light scattered by a surface with a Gaussian-profiled roughness, R_{scat}, at wavelength λ is given by:

$$R_{scat} = R_0 \cdot \exp(-4\pi\sigma^2/\lambda), \quad (1)$$

where R_0 is the ideal reflectance of a flat surface given by Fresnel's equations [51], and σ the RMS roughness. In the case of nanoPS, with roughness values below 2 nm, the scattered light is less than 0.25%, which can be neglected for practical purposes since it is lower than the accuracy of most optical characterization systems.

Optical properties

Given the strong dependence of the structure and morphology of PS on the formation conditions, the optical properties of PS are also greatly influenced by the fabrication parameters. The influence of substrate resistivity on the optical properties of PS has been studied in [52]. Figure 9 shows the reflectance spectra of PS layers formed under the same conditions from differently doped p-type wafers. It is observed that the more heavily doped substrates behave in the ultraviolet in a similar way that bulk silicon, indicating a higher degree of crystallinity of the PS layers.

As discussed in "Structure and morphology" section, PS layers formed under the appropriate conditions may be described as an homogeneous mixture of silicon crystallites, amorphous silicon, and air (pores), with typical feature sizes well below the wavelength of infrared and visible light. Thus, in this wavelength range, the optical properties of nanoPS will mainly depend on the composition of this mixture, that is, on porosity. The optical constants of nanoPS may, in this case, be approximated using effective medium approximation models (EMA) [53–55], being Bruggeman's the most commonly used. The dependence of the refractive index with porosity according to the different models is provided in Fig. 10. Thus, by carefully controlling the porosity of nanoPS, it is possible to adjust its refractive index. In theory, it should be possible to obtain any refractive index between 1 (corresponding to a 100% porosity layer) and the refractive index of silicon (0% porosity). However, this interval is reduced due to the limited range of porosity that can be achieved in practice. This range of porosity, and hence of achievable refractive

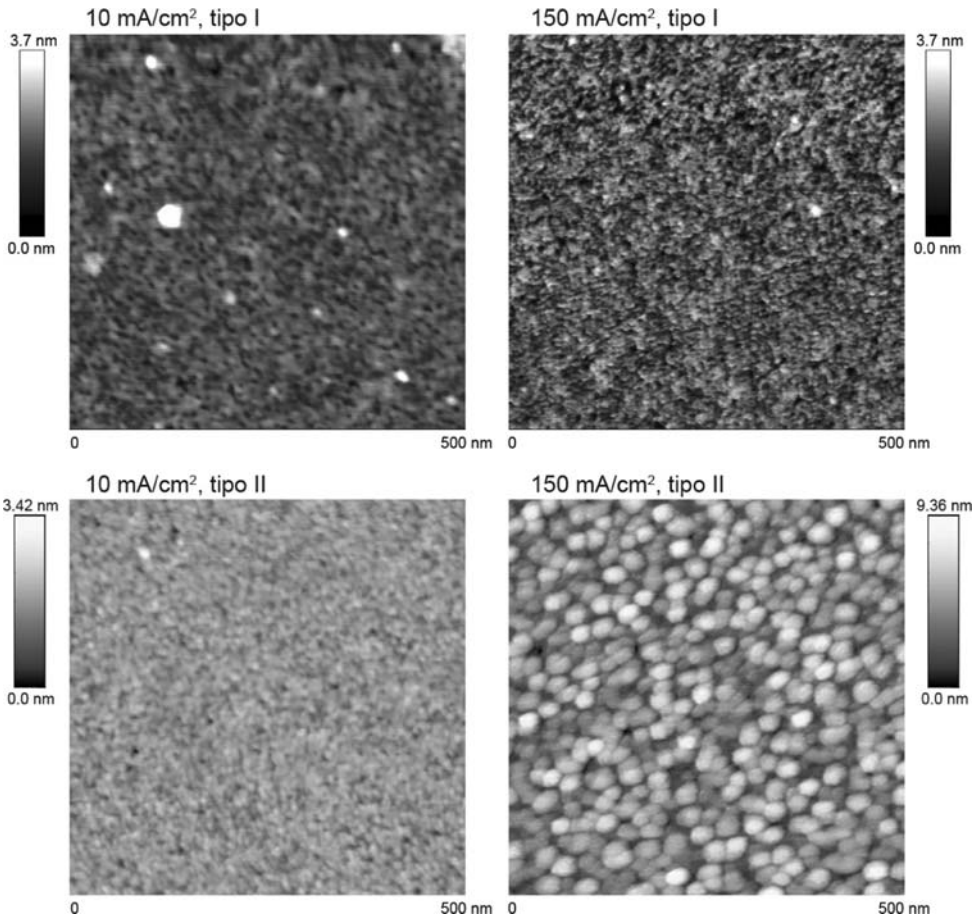

Fig. 8 Atomic force microscopy (AFM) images of the surface of low-porosity (*left*) and high-porosity (*right*) PS layers for different electrolyte compositions: HF to ethanol 2:1 (*up*) and 1:1 (*down*), after [48]

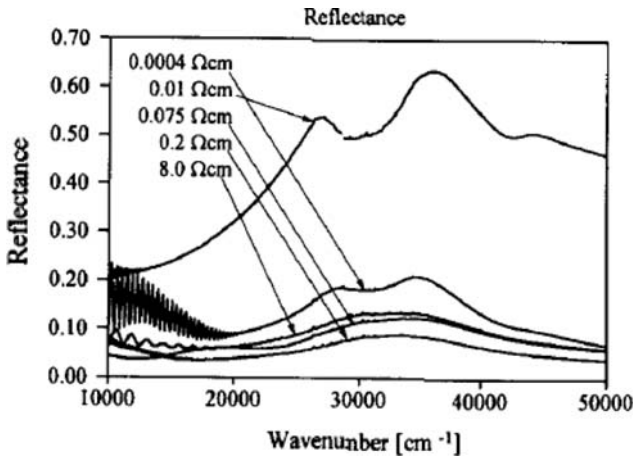

Fig. 9 Reflectance spectra of PS layers formed at 20 mA/cm^2 on differently doped wafers, reproduced from [24] with permission from Elsevier

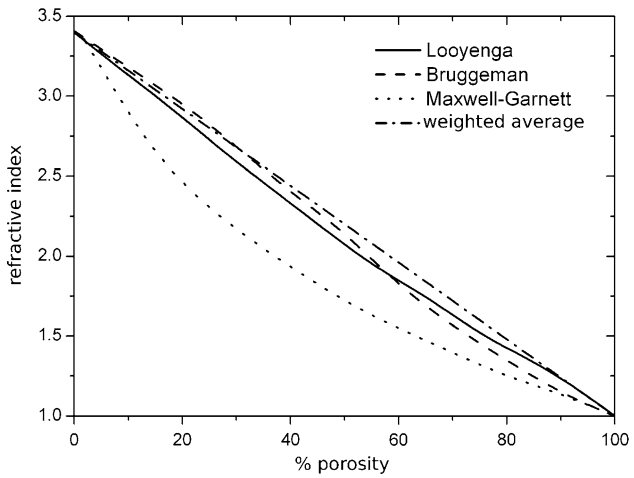

Fig. 10 Dependence of the refractive index with porosity, according to different EMAs, after [53–55]

index, is determined by the lowest porosity that allows proper diffusion of the electrolyte during the etching process to produce homogeneous layers, and the highest porosity that yields a mechanically stable layer.

The optical constants (n, index of refraction and k, extinction coefficient) of PS are usually numerically determined from reflectance [56, 57] or ellipsometry [58, 59] measurements, since their theoretical calculation with any of the EMAs does not usually yield precise results, mainly due to an oversimplification of the mixture model and to uncertainties in the porosity value. Experimental results show that the refractive index of nanoPS decreases

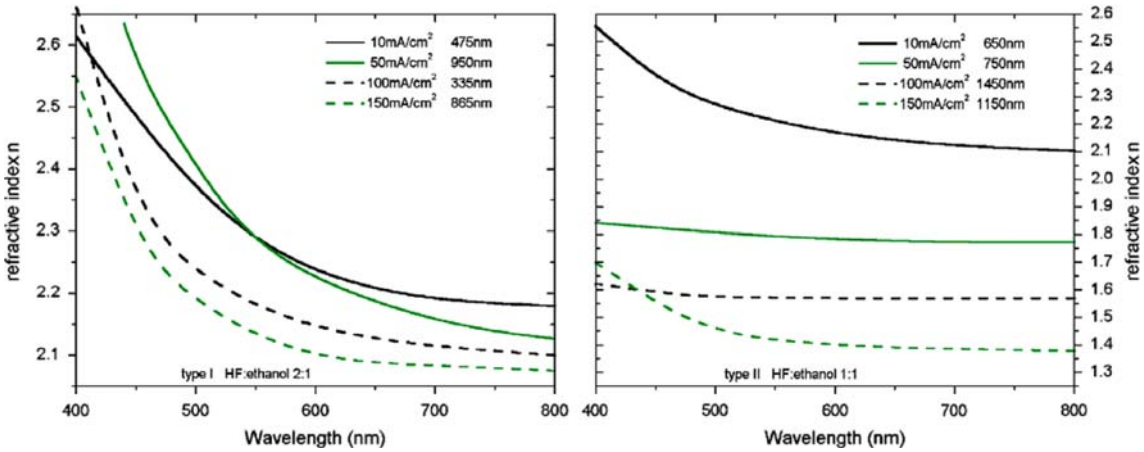

Fig. 11 Refractive index of nanoPS layers fabricated with different current densities, for two electrolyte compositions: HF to ethanol 2:1 (*left*) and 1:1 (*right*). Reproduced from [57] with kind permission from Springer Science + Business Media

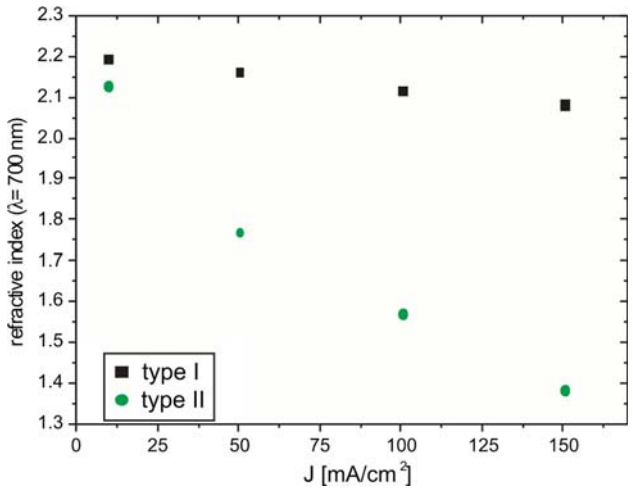

Fig. 12 Refractive index of PS at 700 nm formed with different electrolyte composition (type I: HF:ethanol 2:1, type I: HF:ethanol 1:1), as a function of current density [57]. Reproduced with kind permission from Springer Science + Business Media

with increasing anodization current density (Fig. 11), as a consequence of higher porosity.

The influence of HF concentration in the electrolyte on the refractive index of nanoPS is depicted in Fig. 12 [57]. A lower HF content reduces the electrolyte's viscosity and facilitates its diffusion into the porous structure, favoring the dissolution process and leading to layers of higher porosity. As a consequence, for a given range of current densities, a wider interval of refractive indexes is achievable with lower HF concentration. On the other hand, a higher HF content allows a finer tuning of the optical constants. The absorption coefficient of nanoPS, which is related to the extinction coefficient, also decreases with porosity, as expected from lower silicon content and a finer structure that results in reduced scattering. Additionally, the smaller silicon crystals obtained with higher current densities, show enhanced

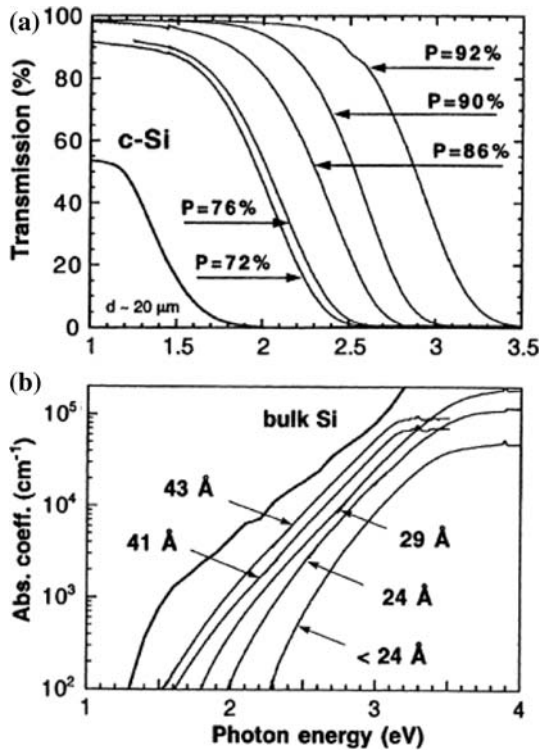

Fig. 13 Transmittance spectra (*top*) and absorption coefficient (*bottom*) of PS free standing layers for increasing porosity. Reproduced from [61] with permission from Elsevier

quantum confinement effects that widens the band gap and blueshifts the absorption edge, further reducing absorption losses in the visible range [1, 60, 61], as shown in Fig. 13.

Multilayer structures

As mentioned earlier in "Fabrication and general properties" section, one major advantage of the electrochemical

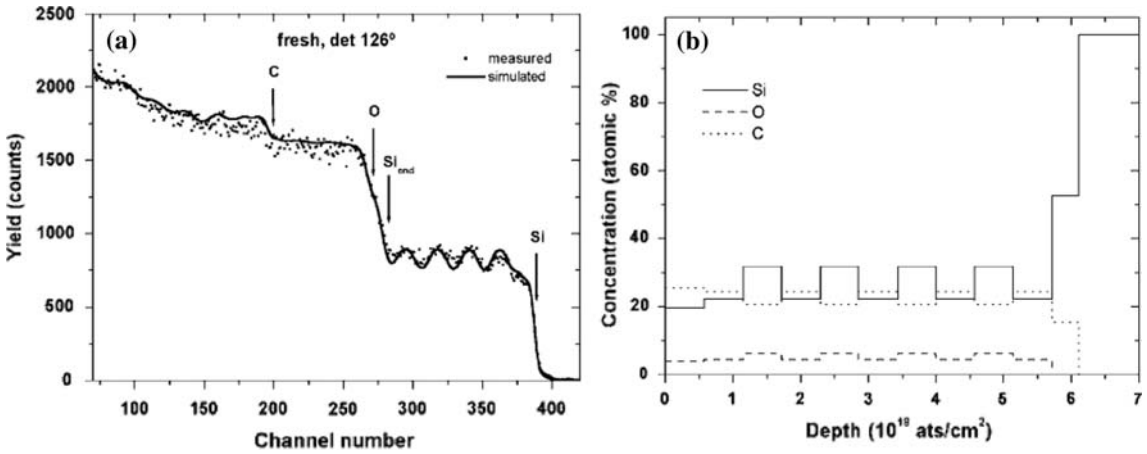

Fig. 14 **a** Typical RBS spectrum of a PS multilayer stack formed by 5-low-porosity/high-porosity periods. **b** Compositional profile obtained from the fit of (**a**). Reproduces from [62] with permission from The Electrochemical Society

etching process for fabricating nanoPS is the ease of fabrication of multilayer structures by simply adjusting the anodization current density during the process. Cross-sectional electron microscopy images (Fig. 3) show that these structures have a notable lateral and in-depth homogeneity, with well defined and sharp interfaces between adjacent layers [17, 18]. In-depth compositional homogeneity has been revealed by RBS [62], from which high- and low-porosity layers are clearly visible, as shown in Fig. 14a. RBS compositional profiles also reveal the same transition layer between PS and the substrate that has been reported in the case of individual layers (Fig. 14b).

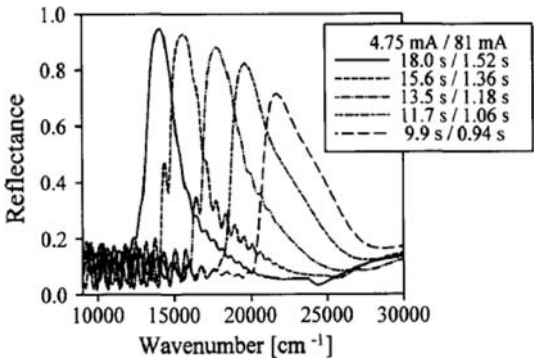

Fig. 15 Example of different nanoPS Bragg reflectors formed under different conditions, showing reflectance peaks in the visible range [24]. Reproduced with permission from Elsevier

Devices and applications

In the following subsections, several applications of nanoPS will be discussed.

Interference filters

The precise optical characterization of the individual nanoPS layers, correlating both refractive index and etch rate with formation parameters, allows the prediction of the interference effects of nanoPS-based multilayer stacks. One of the most common and straightforward interference filter is the Bragg reflector, consisting in a stack of alternating high index and low index quarter-wave layers. This layout leads to the formation of interference filters with a reflectance peak (stop-band) centered at the wavelength where the quarter-wave condition is met. In this way, different filters can be formed with the possibility of tuning the reflectance peak along the whole visible wavelength range by appropriately designing the structure, as shown in Fig. 15.

Figure 16 shows the spectra of nanoPS Bragg reflectors formed with different HF content in the electrolyte [57]. In the two cases (HF to ethanol ratios 2:1 and 1:1), it is observed that the reflectance peak is fully tunable over the whole visible range for either electrolyte composition.

By comparing the spectra of both types of structures, it can be clearly observed that structures formed with a 2:1 HF:ethanol electrolyte show narrower peaks than those formed in an 1:1 HF:ethanol solution. As shown in "Optical properties" section, a lower HF content allows a larger refractive index interval, which results in interference filters with a wider stop-band. This result is expected, since it can be demonstrated [63] that the half width at half maximum $\Delta\lambda$ of a stop-band centered at wavelength λ_0 depends on the high n_H and low n_L refractive indexes as given by:

$$\Delta\lambda = \frac{2\lambda_0}{\pi}\arcsin\left(\frac{n_H - n_L}{n_H + n_L}\right). \quad (2)$$

Another feature of great significance is the peak height, since it is directly related to the overall optical performance

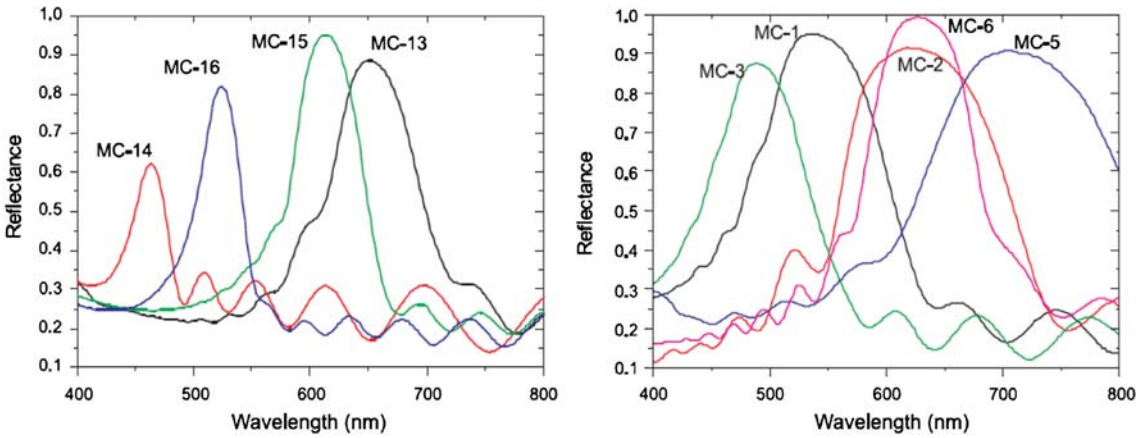

Fig. 16 Reflectance spectra of PS Bragg reflectors formed under different conditions as to tune the reflectance stop-band along the visible range, using two different electrolyte compositions: HF to ethanol 2:1 ratio (*left*), and 1:1 ratio (*right*) [57]. Reproduced with kind permission from Springer Science + Business Media

of the filters. From Fig. 16, it is observed that multilayers formed with a lower HF concentration show higher reflectance peaks. This behavior is attributed to a higher porosity of nanoPS, as discussed in "Optical properties" section. As reported elsewhere, increasing porosity leads to a blue shift of the absorption edge [1, 61] as a consequence of the band gap widening due to quantum confinement effects, resulting in less absorption losses, especially for wavelengths below 500 nm.

Filtered light emitting devices

The photoluminescence (PL) spectrum of PS has been reported to posses a typical width at half maximum (FWHM) of around 200 nm [1]. Such a broad spectrum is not appropriate for practical applications where high monochromaticity is often required, or in optical sensing applications. In order to reduce the width of the PL emission spectrum, a luminescent nanoPS layer is placed between two Bragg reflectors, forming a microcavity structure [56]. The reflectance spectrum of this structure consists in a sharp reflectance dip at the resonant wavelength, surrounded by two Bragg reflection bands. This reflectance dip corresponds to a transmittance peak for light originated at the luminescent resonant layer. Hence, only the PL emission within this narrow wavelength range will finally reach the surface and escape. Figure 17—left presents a schematic view of a typical microcavity structure, designed to show a resonant peak around 750 nm, while Fig. 17—right shows the reflectance and PL spectra of such a device, consisting on a 480 nm luminescent layer sandwiched between two 3-period Bragg reflectors, having each one a total thickness of 575 nm approximately.

The resonant peak can be observed around 744 nm, with an FWHM of about 40 nm. Interestingly, the PL emission of this device is much narrower than that of bare PS [1]. As expected, the filtered PL peak matches the dip of the

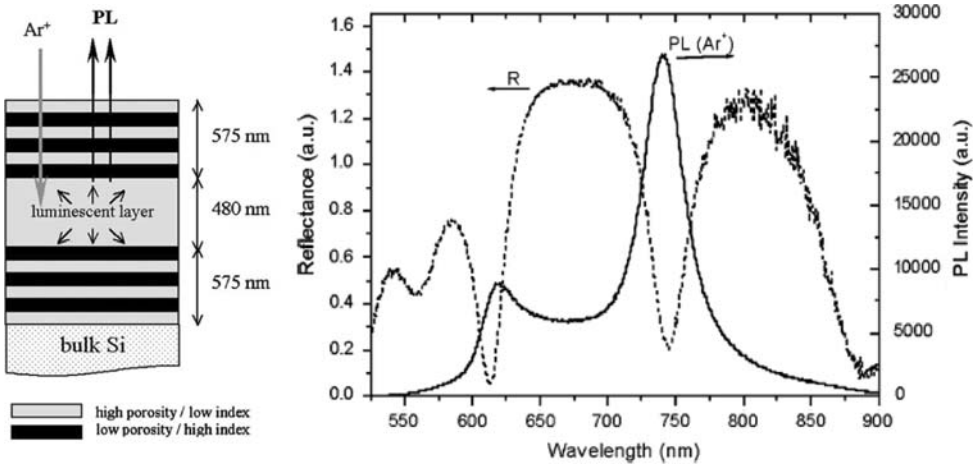

Fig. 17 Schematic of a Fabry-Pérot filtered photoluminescent PS device (*left*), and its corresponding reflectance and PL spectra (*right*). Reproduced from [72] with permission from Elsevier

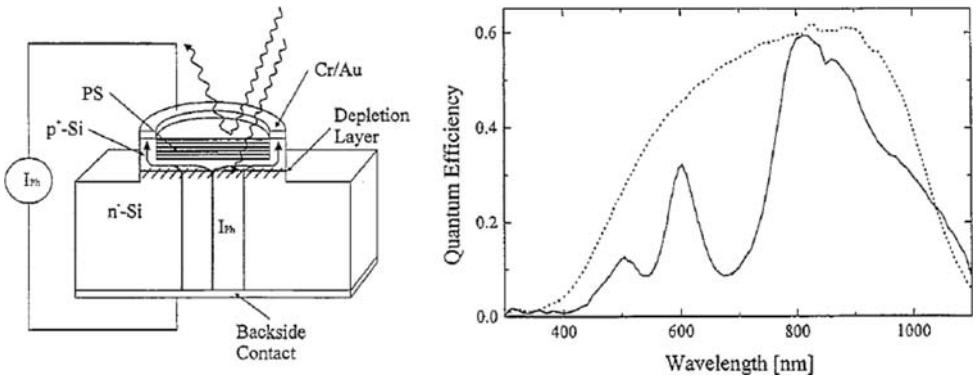

Fig. 18 *Left*: schematic of a PS-filtered silicon photodiode. *Right*: efficiency spectrum (*solid*), compared to that of unfiltered Si photodiode (*dashed*) [65]. Reproduced with permission from Elsevier

reflectance spectrum. A secondary PL peak can be observed around 620 nm, corresponding to the end of the high reflectance region, which still overlaps the high energy tail of the photoluminescence spectrum. A slight PL background can be observed across the whole spectrum. This is caused by the high-porosity layers forming the top reflector, which are also photoluminescent. The background may be minimized reducing the porosity of these layers, since porosity is directly related to crystallite size and hence, to the PL intensity of PS due to quantum confinement effects [1, 16, 27]. However, reducing the porosity of the high-porosity layer (hence, increasing its refractive index) directly affects the performance of the Bragg reflector, since the refractive index mismatch between the low- and high-index layers is also reduced. It should be taken into account that the objective lenses used in these measurements have a finite optical aperture and, in consequence, both the reflectance and PL spectra are integrated over a small detection angle, which leads to a convolution of the spectra. Sharper, unconvoluted spectra have been obtained using optical fibers for both excitation and light collection.

Filtered photodetectors

NanoPS optical filters may also be used to enhance the spectral performance of silicon photodiodes. In a metal–nanoPS–Si heterojunction, no depletion is expected at the metal–nanoPS junction due to the high density of states in the porous layer, which locks the Fermi level. Band bending should occur, however, inside the silicon substrate at the nanoPS–Si junction [64]. In this way, photoresponse is only expected when this latter junction is illuminated. In the visible range, nanoPS has a low absorption coefficient [57, 61], which means that in a metal–nanoPS–Si structure, the porous layer acts as a semi-transparent window over the Si substrate. Thus, the nanoPS layers modulate the spectral photoresponse of the Si substrate according to their transmittance spectrum, as first shown by Krüger et al. [65]. Figure 18 shows an schematic view of a silicon photodiode with a nanoPS Fabry-Pérot filter, and its efficiency curve.

Filtering of the response curve has been improved using double-Bragg band pass filters like that shown in Fig. 19—left [66]. By comparing the response curve of such device with its reflectance spectrum (Fig. 19—right) it can be

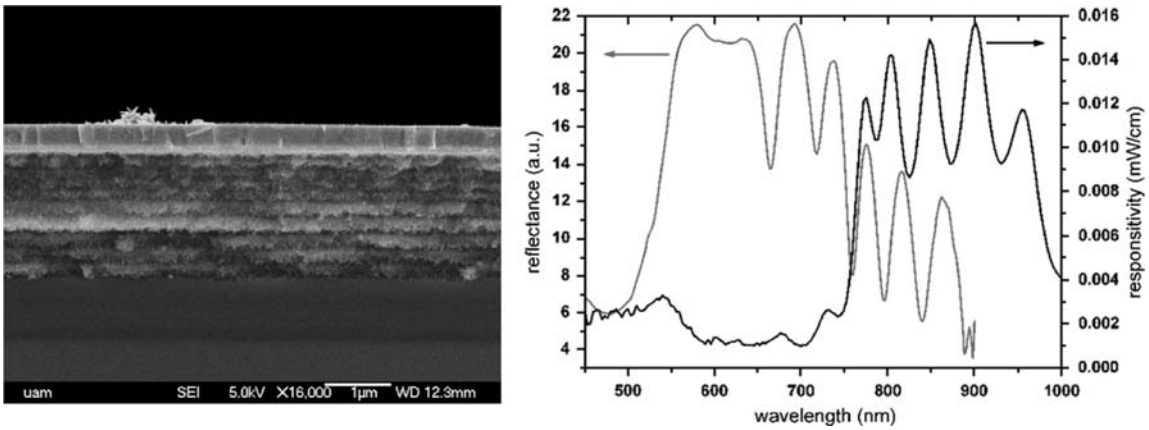

Fig. 19 Cross-sectional SEM view of a PS-filtered Si photodiode, showing the double-Bragg filter (formed by two 5-period Bragg reflectors), and the top ITO transparent contact (*left*). Reflectance and responsitivity spectra of such a device (*right*). Reproduced from [66] with permission from Elsevier

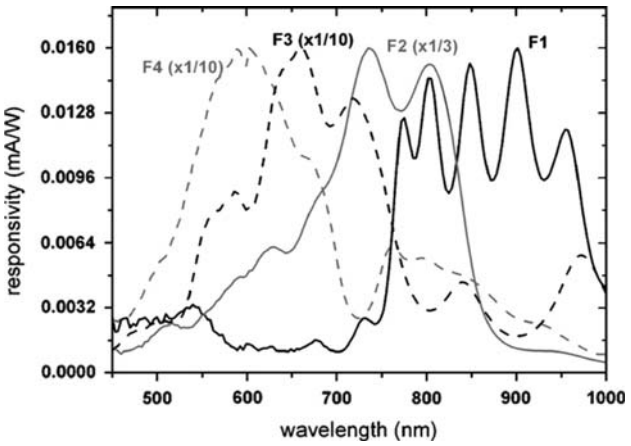

Fig. 20 Responsivity spectra of different PS-filtered photodiodes: the response peak is tunable across the silicon photoresponse range, between 500 and 1,100 nm [66]. Reproduced with permission from Elsevier

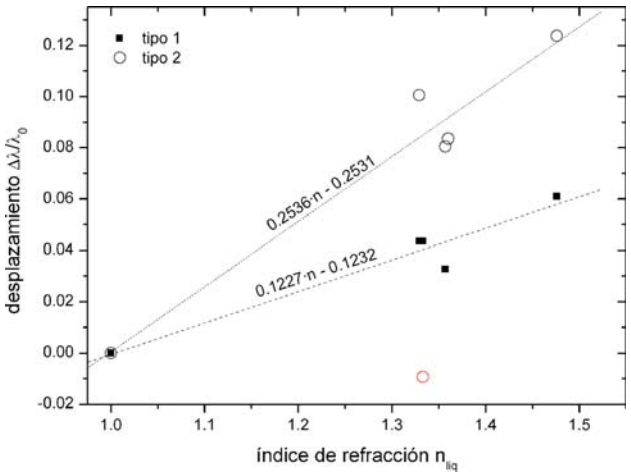

Fig. 21 Redshift of a nanoPS Bragg reflector after infiltration with a liquid of refractive index n_{liq}, for two different multilayer designs: one with a higher average porosity (*open circles*), and the other with a lower average porosity value (*full circles*), after [48]

observed that, as expected, high reflectance peaks correspond with low-responsitivity dips and vice versa.

The spectral responsitivity of these devices is much narrower than that of bulk silicon, down to 150 nm approximately. Moreover, the responsitivity peak is fully tunable, depending on filter design, from 500 to 1,100 nm as shown in Fig. 20. Below 500 nm, no photocurrent is detected due to the low responsitivity of crystalline silicon (Fig. 18—right) and the higher absorption losses in the PS filter.

Chemical sensors

Since PS can be described in the visible wavelength range as a homogeneous mixture of silicon and air, the effective refractive index of nanoPS will depend on the relative air content of the mixture. If pores are filled by other substances, the effective refractive index of the mixture is increased, resulting in a redshift of the optical spectrum. Applying a simple EMA, the refractive index of PS n_{PS} may be expressed as:

$$n_{PS} = p + (1 - p) \cdot n_{Si}, \tag{3}$$

where p is the porosity of the sample and n_{Si} the refractive index of bulk silicon. In this model, if the pores are infiltrated by a substance of refractive index n_{inf}, the new effective refractive index of nanoPS will be given by:

$$n_{PS^*} = p \cdot n_{inf} + (1 - p) \cdot n_{Si}, \tag{4}$$

which results in a refractive index increase, Δn, given by:

$$\Delta n = p \cdot (n_{inf} - 1). \tag{5}$$

In the case of a Bragg reflector, or any other interference filter, this increase in the average refractive index produces a redshift of the optical spectrum given by:

$$\Delta\lambda/\lambda_0 = \Delta n = p \cdot (n_{inf} - 1). \tag{6}$$

Figure 21 shows the reflectance spectrum of a typical as-prepared Bragg reflector, and the same device after infiltration with different liquids. As expected, a clear redshift of the reflectance maximum with infiltration can be observed. It is important to notice that the redshift is proportional to the refractive index of the liquid filling the pores, as previously shown by Mulloni et al. [67], and to the average porosity of the structure [48].

The high reactivity of the internal surface of nanoPS makes that not only full filling of the pores by liquids can be monitored, but also partial filling or surface adsorption by different vapors can be optically detected. Results for different gases and concentrations are shown in Fig. 22.

In addition to the spectral shift, it is observed that the overall shape of the spectra is also slightly altered, especially the stop-band width [68]. Figure 23 shows the full width at half maximum variation of the reflectance stop-bands under different vapor species and concentrations.

Vapor-induced spectral alterations may be used to provide optical sensors with selectivity. From Fig. 23, it is noticed that there is no significant difference in the observed redshift of the reflectance spectra stop-band, when the reflector is subjected to acetone and methylamine vapors. However, regarding stop-band alteration, it can be noted that acetone causes an increase in the FWHM value, whereas a decrease is observed for methylamine. These changes in the FWHM may be attributed to a different behavior of the adsorbate gas molecules. The stop-band width, as explained in "Interference filters" section, depends on the high- and low-refractive index mismatch according to Eq. 2. The high-index layers result from a lower etching current density, which also produces smaller

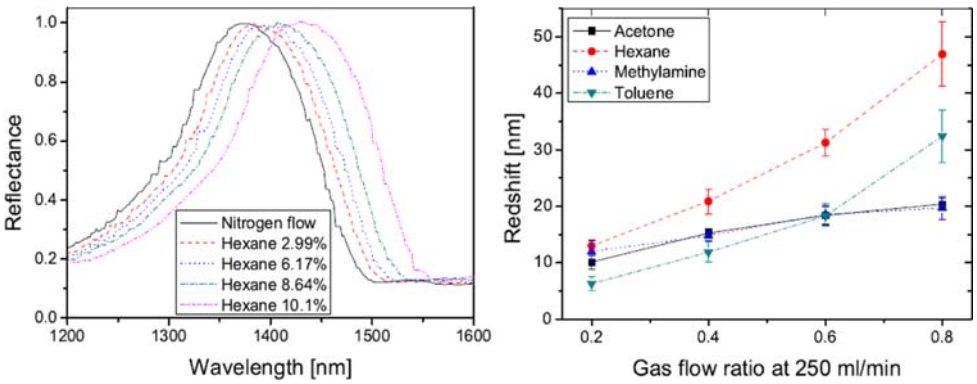

Fig. 22 Redshift of a nanoPS Bragg reflector upon increasing exposure to hexane vapor (*left*), and to other hydrocarbon species (*right*). Reproduced from [68] with permission

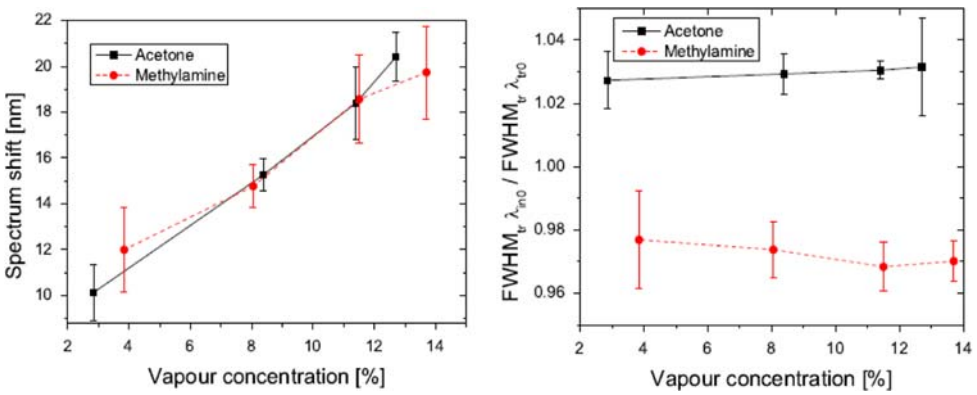

Fig. 23 Spectral redshift (*left*) and change in peak width (*right*) of a porous silicon Bragg reflector when exposed to increasing concentrations of acetone and methylamine. Note that, despite the two substances produce a similar redshift, their effect on the reflectance peak width is different. Reproduced from [68] with permission

pores. Therefore, some adsorbate molecules might have a higher affinity to either larger or smaller pore layers, affecting differently the refractive index of either layer and explaining the observed changes in the stop-band width. In this way, the behavior observed for acetone and methylamine in Fig. 23, could be explained by assuming that both vapors produce the same change in the overall refractive index of the structure, but affect high- and low-index layers differently, thus yielding a similar spectrum shift, but different alteration of the stop-band width.

Biosensors

Porous silicon-based biosensors based on optical interferometry have been fabricated. These devices have been reported to allow the detection of small organic molecules at pico- and femtomolar analyte concentrations [69]. The operational principle is based on induced shifts of interference fringes of appropriately derivatized thin films of PS. Binding of molecules induced changes in the refractive index of PS. Accordingly, in the presence of complementary DNA (cDNA) sequences, pronounced wavelength shifts in the interference pattern of the PS thin films are induced (Figs. 24, 25). Under similar conditions but in the presence of non-cDNA sequences, no significant shift in the wavelength of the interference fringe pattern is detected (only minor amplitude fluctuations are observed). This type of optical biosensor has also been demonstrated to be highly effective for detecting single and multilayered molecular assemblies. In addition to these structures, microcavity resonators made of PS have been used as biosensors and demonstrated in DNA detection. Such microcavity structures are highly sensitive and any slight change in the effective optical thickness modifies its reflectivity spectrum, causing a spectral shift in the interference peaks. This makes PS microcavities an ideal host for biosensor applications.

Furthermore, nanoPS-based microcavities have been developed for their use as biosensors, by exploiting the luminescent properties of nanoPS [70]. As described in "Filtered light emitting devices" section, microcavity resonators possess the unique characteristics of line narrowing and intensity enhancement of photoluminescence from nanoPS layers. The emission peak position can be tuned by changing the properties of the central layer. Increasing the thickness of the central active layer, for example, introduces multiple narrow peaks in the luminescence spectrum. Narrow and visible luminescence peaks are observed with an FWHM value of 3 nm. The usefulness of microcavity resonator structures as biosensors was demonstrated by fabricating a DNA biosensor based on a nanoPS multiple peak microcavity structure. Shifts in the luminescence

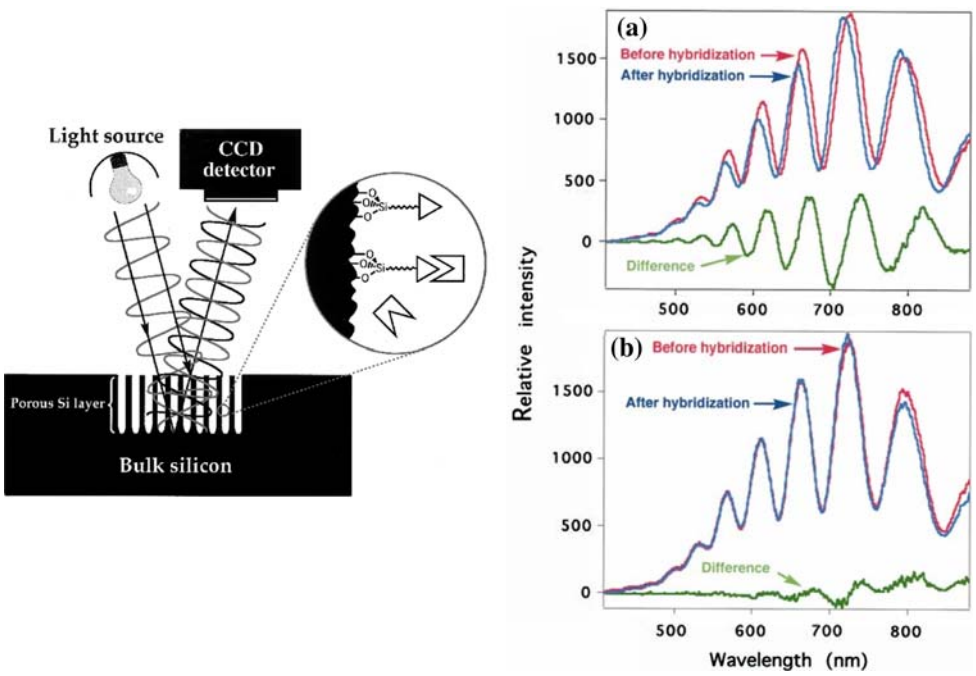

Fig. 24 Principle of operation of an optical porous silicon DNA biosensor. Reproduced from [69] with permission from the AAAS

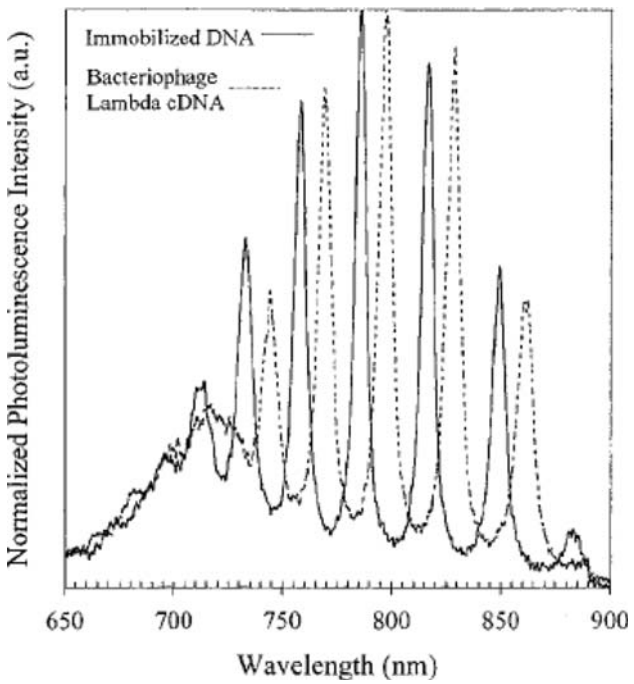

Fig. 25 DNA porous silicon biosensor. The microcavity filters the wide photoluminescence emission of nanoPS to narrow peaks. The detection of DNA changes the filter's properties, resulting in a noticeable shift in the PL spectrum. Reproduced from [70] with permission

spectra are observed and detected for various DNA concentrations. When exposed to a non-complementary DNA strand, no shifts are observed.

Conclusions

In the last two decades, nanoPS has been thoroughly studied. The relative easiness of fabrication of this material, along with the possibility of precisely controlling its many peculiar properties, has made of PS a promising material for application in a wide variety of fields.

In particular, the optical properties of PS have devoted a large amount of interest. The tunability of its refractive index, along with the possibility of fabricating layered structures, allows the development of a broad variety of optical interference devices operating in the visible and infrared ranges, including communication wavelengths, based on silicon and integrable into conventional microelectronic systems. Optical PS devices have been successfully implemented in different optoelectronic devices, including filtered light emitters and tuned photodetectors.

Furthermore, the high internal surface and peculiar physico-chemical properties of PS have allowed the realization of different sensing devices. Liquid and gas optical sensors have been developed, exploiting the sensitivity of the optical response of PS to its physico-chemical environment. Moreover, PS optical filters and light emitting devices have been successfully used to develop highly sensitive optical biosensors, taking PS to the field of medical and biochemical applications.

Current research on nanoPS comprises diverse fields and applications. In the photonics field, patterning of PS is being employed to develop 2D and 3D photonic crystals for light manipulation. Also, PS is being actively studied for biological and medical applications. To cite two

examples, biofunctionalized PS structures are being studied as scaffolds to study cellular processes, and PS microparticles are already being used for localized drug delivery.

Thus, it is expected that in the near future nanoPS will find applications in a number of fields, by exploiting not only its optical properties, but also its many other peculiar characteristics, such as ease of fabrication, high internal surface or chemical reactivity, all this from a silicon-based, industry-compatible material.

Acknowledgements Partial funding was provided by the Spain's National R&D Programme through grant no. MAT2008-06858-C02-01/NAN. Authors wish to thank T. Jälkanen and J. Salonen from the University of Turku (Finland) for fruitful discussion regarding the optical gas sensors, and Mr. Luis G. Pelayo for his technical contribution to this work.

References

1. Canham LT (1990) Appl Phys Lett 57(10):1046
2. Halimaoui A, Oules C, Bromchil G, Bsiesy A, Gaspard F, Herino R, Ligeon M, Muller F (1991) Appl Phys Lett 59(3):304
3. Koshida N, Koyama H (1992) Appl Phys Lett 60(3):347
4. ISI Web of Knowledge (http://www.isiknowledge.com), accessed on September 2009
5. Uhlir A (1956) Bell Syst Technol J 35(2):333
6. Watanabe Y, Sakai T (1971) Rev Electron Commun Labs 19(7–8):899
7. Otoi F, Anzai K, Kitabayashi H, Uchiho K, Mizokami Y (1984) J Electrochem Soc 131(8):C319
8. Turner DR (1958) J Electrochem Soc 105(7):402
9. Archer RJ (1960) J Phys Chem Solids 14:104
10. Hummel RE, Chang SS (1992) Appl Phys Lett 61(16):1965
11. Saadoun M, Mliki N, Kaabi H, Daoudi K, Bessais B, Ezzaouia H, Bennaceur R (2002) Thin Solid Films 405(1–2):29
12. Carstensen J, Christophersen M, Lolkes S, Ossei-Wusu E, Bahr J, Langa S, Popkirov G, Föll H (2005) Phys Stat Solid C 2(9):3339
13. Rieger MM, Kohl PA (1995) J Electrochem Soc 142(5):1490
14. Allongue P, Kieling V, Guerischer H (1995) Electrochim Acta 40(10):1353
15. Rao AV, Ozanam F, Chazalviel JN (1991) J Electrochem Soc 138(1):153
16. Gerischer H (1990) Electrochim Acta 35(11–12):1677
17. Beale MIJ, Benjamin JD, Uren J, Chew NG, Cullis AG (1985) J Cryst Growth 73(3):622
18. Smith RL, Collins SD (1992) J Appl Phys 71(8):R1
19. Dittrich Th, Yu Timoshenko V, Rappich J (2001) J Appl Phys 90(5):2310
20. Berger MG, Dieker C, Thönissen M, Vescan L, Lüth H, Münder H (1994) J Phys D 27(6):1333
21. Frohnhoff St, Berger MG, Thömissen M, Dieker C, Vescan L, Münder H, Lüth H (1995) Thin Solid Films 255(1–2):59
22. Steckl A, Xu J, Mogul H, Prokes S (1995) J Electrochem Soc 142:L69
23. Torres-Costa V, Martín-Palma RJ, Manotas S, Agulló-Rueda F, Martínez-Duart JM (2004) Bol Soc Esp Cerám Vidrio 43(2):506
24. Theiss W (1997) Surf Sci Rep 29:91
25. Lehmann V (2002) Electrochemistry of silicon. Instrumentation, science, materials and applications. Wiley-VCH, Weinheim
26. Labunov V, Bondarenko V, Glinenko L, Dorofeev A, Tabulina L (1986) Thin Solid Films 137:123
27. Barla K, Bomchil G, Herino R, Pfister JC, Baruchel J (1984) J Cryst Growth 68:721
28. Munder H, Andrzejak C, Berger MG, Klemradt U, Luth H, Hérino R, Ligeon M (1992) Thin Solid Films 221(1–2):27
29. Bellet D, Dolino G (1996) Thin Solid Films 276:1
30. Martín-Palma RJ, Pascual L, Herrero P, Martínez-Duart JM (2005) Appl Phys Lett 87:211906
31. Campbell IH, Fauchet MP (1986) Solid State Commun 58:739
32. Mariotto G, Ziglio F, Freire FL Jr (1995) J Non-Cryst Solids 192/193:253
33. Manotas S, Agulló-Rueda F, Moreno JD, Martín-Palma RJ, Guerrero-Lemus R, Martínez-Duart JM (1999) Appl Phys Lett 75(7):977
34. Sui Z, Leong PP, Herman IP, Higashi GS, Temkin H (1992) Appl Phys Lett 60(17):2086
35. Munder H et al (1992) Thin Solid Films 22:27
36. Frohnhoff St, Marso M, Berger MG, Thonissen M, Luth H, Mender H (1995) J Electrochem Soc 142(2):615
37. Lehmann V, Jobst B, Muschik T, Kux A, Petrova-Koch V (1993) Jpn J Appl Phys 32(5):2095
38. Cullis AG, Canham LT (1991) Nature 353:335
39. Martín-Palma RJ, Pascual L, Landa A, Herrero P, Martínez-Duart JM (2004) Appl Phys Lett 85(13):2517
40. Martín-Palma RJ, Pascual L, Herrero P, Martínez-Duart JM (2002) Appl Phys Lett 81(1):25
41. Hirsch P, Howie A, Nicholson RB, Pashley DW, Whelan MM (1997) Electron microscopy of thin crystals. Krieger, Melbourne
42. Torres-Costa V, Martın-Palma RJ, Pászti F, Climent-Font A, Martínez-Duart JM (2006) J Non-Cryst Solids 352(23–25):2521
43. Williams DB, Carter CB (1996) Transmission electron microscopy. Plenum Press, London
44. Barla K, Hérino R, Bomchil G, Pfister JC, Freund A (1984) J Cryst Growth 68:727
45. Buttard D, Bellet D, Dolino G (1996) J Appl Phys 79:8060
46. Laiho R, Pavlov A, Pavlova Y (1997) Thin Solid Films 297:138
47. Pavlov A, Pavlova Y (1997) Thin Solid Films 297:132
48. Torres-Costa V (2006) PhD thesis, Universidad Autónoma de Madrid, Spain
49. Davies H (1954) Proc Inst Electr Eng 101:209
50. Bennett HE, Porteus J (1960) J Opt Soc Am 51:123
51. Hecht E, Zajac A (1986) Óptica. Addison-Wesley Iberoamericana, Wilmington, p 86
52. Hilbrich S, Theiss W, Arens-Fischer R, Glück O, Berger MG (1996) Thin Solid Films 276:231
53. Bruggeman DAG (1935) Ann Phys 24:636
54. Looyenga H (1965) Physica (Amsterdam) 31:401
55. Bergman DJ (1978) Phys Rev C 43:377
56. Pavesi L (1997) Riv Nuovo Cimento 20:1
57. Torres-Costa V, Martín-Palma RJ, Martínez-Duart JM (2004) Appl Phys A 79(8):1919
58. Basmaji P, Bagnato VS, Grivickas V, Surdutovich GI, Vitlina R (1993) Thin Solid Films 233(1–2):131
59. Zangooie S, Jansson R, Arwin H (1999) J Appl Phys 86(2):850
60. Sagnez I, Halimaoui A, Vincent G, Badoz PA (1993) Appl Phys Lett 62:1155
61. Von Behren J, van Buuren T, Zacharias M, Chimowitz EH, Fauchet PM (1998) Solid State Commun 105:317
62. Torres-Costa V, Pászti F, Climent-Font A, Martín-Palma RJ, Martínez-Duart JM (2005) J Electrochem Soc 152(11):G846
63. Macleod HA (1969) Thin-film optical filters, chap 5. Hilger, London
64. Ben-Chorin M, Möller F, Köch F (1995) J Appl Phys 77(8):4482
65. Krüger M, Marso M, Berger MG, Thönissen M, Billat S, Loo R, Reetz W, Lüth H, Hilbrich S, Arens-Fischer R, Grosse P (1997) Thin Solid Films 297(1–2):241

66. Torres-Costa V, Martín-Palma RJ, Martínez-Duart JM (2007) Mater Sci Eng C 27(5–8):954
67. Mulloni V, Gaburro Z, Pavesi L (2000) Phys Stat Solid A 182:479
68. Jalkanen T, Torres-Costa V, Salonen J, Björkqvist M, Mäkilä E, Martínez-Duart JM, Lehto V-P (2009) Opt Exp 17(7):5446
69. Lin VS-Y, Motesharei K, Dancil K-PS, Sailor MJ, Ghadiri MR (1997) Science 278:840
70. Chan S, Fauchet PM, Li Y, Rothberg LJ, Miller BL (2000) Phys Stat Solid 182:541
71. Martin-Palma RJ, Guerrero-Lemus R, Moreno JD, Martinez-Duart JM, Herrero P (1998) J Mater Sci Lett 17:845
72. Torres-Costa V, Agullo-Rueda F, Martín-Palma RJ, Martínez-Duart JM (2005) Opt Mater 27:1084